Cement and Concrete Research 42 (2012) 778–788

Contents lists available at SciVerse ScienceDirect

Cement and Concrete Research

journal homepage: http://ees.elsevier.com/CEMCON/default.asp

Effect of mechanical activation on the hydraulic properties of stainless steel slags

Lubica Kriskova [a,*], Yiannis Pontikes [a], Özlem Cizer [b], Gilles Mertens [c], Wout Veulemans [a], Daneel Geysen [a], Peter Tom Jones [a], Lucie Vandewalle [b], Koen Van Balen [b], Bart Blanpain [a]

[a] Centre for High Temperature Processes and Sustainable Materials Management, Department of Metallurgy and Materials Engineering, KU Leuven, Kasteelpark Arenberg 44 bus 2450, BE-3001 Heverlee, Belgium
[b] Department of Civil Engineering, KU Leuven, Kasteelpark Arenberg 40 bus 2448, BE-3001 Heverlee, Belgium
[c] Qmineral bvba., Papenkasteelstraat 58, BE-1180 Brussel, Belgium

ARTICLE INFO

Article history:
Received 26 September 2011
Accepted 23 February 2012

Keywords:
Stainless steel slag
Characterization (B)
Hydration (A)
Microstructure (B)
X-ray diffraction (B)

ABSTRACT

This work aims to assess the possibility of using ladle metallurgy and argon oxygen decarburization stainless steel slag as a hydraulic binder after mechanical activation. Prolonged milling in ethanol suspension resulted in 10-fold increase of the surface area and increase of the amorphous phase. Calorimetric analysis of slags mixed with water indicated the occurrence of exothermic reactions. XRD results revealed that periclase, merwinite, γ-C_2S and bredigite, decreased with hydration time. Thermogravimetric analyses indicated that the main hydration products are most probably C–S–H, CH and MH. The hydrated products in both slags were similar to C–S–H gel. WDS analysis demonstrated Ca and Si to be widespread in the structure. Formation of M–S–H gel or incorporation of Mg in the C–S–H gel remains uncertain. The 90 days compressive strength of mortars prepared from slags reached approximately 20% for LM and 10% for AOD of the compressive strength of mortars prepared from OPC.

1. Introduction

Stainless steel slags include EAF (Electric Arc Furnace), AOD (Argon Oxygen Decarburization) and LM (Ladle Metallurgy) slags. The last two types of slags are generated during the basic refining process step in stainless steelmaking. The quantity produced in 2010 amounts to 10.4 Mt [1,2]. Although the chemical composition of these slags is highly variable, both AOD and LM slags are Ca-, Si- and Mg-rich. The main minerals typically found in these slags are dicalcium silicate (Ca_2SiO_4) — usually the gamma polymorph, merwinite ($Ca_3Mg(SiO_4)_2$), bredigite ($Ca_7Mg(SiO_4)_4$) and periclase (MgO) [3]. Dicalcium silicate (C_2S) undergoes a series of polymorphic transformations upon cooling; of particular interest in the present study is the β-C_2S to γ-C_2S transformation at 490 °C [3–6]. It is accompanied by a volume increase of approximately 10% and results into shattering of the crystals [3,7–12]. Finally, up to 35 wt.% of the ladle slag consists of particles less than 75 μm [3].

In industry, one of the most common ways to tackle the formation of fines is by the addition of borates [10] resulting in the stabilisation of β-C_2S. However, even when C_2S is stabilised, free lime (CaO) and magnesia (MgO) may cause severe problems due to swelling or volume expansion when in contact with water. Nonetheless, post-treatment of slags can contribute in their volume stability and various steel slags are being valorised. The main application fields are in the production of aggregates for road construction purposes, in cement production, in the production of fertilisers, for use as armour stones in hydraulic engineering as well as for internal recycling operations in the steel works [8,13–17]. In the quest of higher value applications, the valorisation of slag as a binder seems to be a potentially promising field.

With a production of 0.97 t of CO_2 per ton of clinker [12], which corresponds to approximately 5%–8% of the total anthropogenic CO_2 emissions [18,19], the cement industry is investigating possible revisions in the manufacturing process and in the selection of raw materials. On the "Cement Technology Roadmap 2009" [20], possible transition paths for the industry are presented in order to reduce the global CO_2 emissions by 50% in 2050. Reducing the clinker content in cement (the "clinker to cement ratio", or "clinker factor") is one of the primary paths. The use of stainless steel slag as a supplementary cementitious material can be of great interest in this context. Indeed, even though stainless steel slag production is an insignificant fraction compared to the almost 3 billion tonnes of annual global cement production [21], it is of interest for specific regions, Europe, being one.

The potential of secondary steelmaking slag to be used as hydraulic binders has been investigated before. Sheh et al. [1] mentioned the phenomenon of particle size growth on ground stainless steel AOD slag when mixed with water and suggested it indicates pozzolanic or hydraulic properties. Ruyi et al. stated that a composite cement can be formed when a proper amount of stainless steel AOD slag is added [22]. Faraone et al. [23] claim that steelmaking slag is not an

* Corresponding author at: Kasteelpark Arenberg 44 bus 2450, BE-3001 Heverlee, Belgium. Tel.: +32 16 321318; fax: +32 16 321991.
E-mail address: lubica.kahalova@mtm.kuleuven.be (L. Kriskova).

0008-8846/$ – see front matter © 2012 Elsevier Ltd. All rights reserved.
doi:10.1016/j.cemconres.2012.02.016

inert material whereas Setién et al. [7] observed that LM slag developed cementitious properties when it reacted with atmospheric moisture. Rodriguez et al. [16] used LM slag in masonry mortars as a partial replacement for sand and cement. Finally, Shi et al. studied [3,9] the cementitious properties of chemically activated LM slag. Even though it is difficult to make general statements regarding the valorisation of steel and stainless steel slag, the cited works do demonstrate a clear potential for these materials.

A possible way to increase the reactivity of stainless steel slags can be though mechanical activation, which, to the best of our knowledge, has not been explored yet. Mechanical activation has been addressed however on a variety of other materials such as granulated blast furnace slag, fly ash, quartz and periclase as a way to improve their reactivity [24–31]. As demonstrated, the high energy milling results in combined effects of increased surface area and structural disorder. This may result in increased amount of grain boundaries, higher density of vacancies and dislocations, stacking faults and pores, alteration of the bond length/ angles/energy, increased energy of electrons and higher oxidation states [25,26]. Metastable phases and enhanced dissolution rates are often the outcome of this prolonged milling [32]. For instance, Kumar et al. [25] observed that the complete hydration of granulated blast furnace slag is possible without any chemical activator if the slag is mechanically activated in an attrition mill. In practise, high-energy milling of cementitious material such as blast furnace slag and fly ash improves the reactivity of the resulting blended cement [28,29] and a higher slag content can be incorporated in the blended slag cement [30].

In the present study, the effect of mechanical activation on the hydraulic properties of two stainless steel slags, namely LM and AOD slags, was studied, aiming to assess the possibility of using these stainless steel slags as hydraulic binders.

2. Materials and experimental methods

The LM and AOD slag used in this investigation were obtained from a producer of ferritic stainless steel. The LM slag was taken from the slag yard, without having been subjected to aging or any other treatment. The AOD slag was taken directly from the converter. The slag is in the form of a fine powder due to the β-C_2S to γ-C_2S transformation. The fraction<125 μm, which comprises approximately 90 wt.% of the total material, was used. The chemical composition was determined using X-ray fluorescence spectrometry (XRF, Philips PW 2400).

Mechanical activation was performed by using a bead mill (Dispermat SL-12-C1, VMA) was used. The milling was carried out with approximately 10 wt.% slag in ethanol suspension at 5000 rpm using 1 mm zirconium balls. To determine the effect of milling time on the powder fineness, the LM slag was milled for 2 h and 6 h. Based on the results obtained in terms of hydraulic reactivity, the AOD slag was only milled for 6 h. The particle size distribution, in both as-received and milled samples, was determined by a laser scattering technique (MasterSizer Micro Plus, Malvern). Each powder was measured three times and the average values were subsequently used for the Rosin-Rammler distribution fit. The surface area of as-received and milled powders was determined by nitrogen sorption method BET (Micromeritics TriStar 3000 V6.04 A) after drying at 150 °C for 12 h.

In order to investigate changes upon milling and hydration, the mineralogy before and after milling and after hydration was determined by quantitative X-ray powder diffraction analysis (QXRPD, D500, Siemens). To avoid affecting the structure of the as-received powders, samples were milled in a McCrone mill for 5 minutes. Diffraction patterns were measured in 2θ range of 10–70° using CuKα radiation of 40 kV and 40 mA, with a 0.01° step size and step time of 3 s. Qualitative analysis was performed by "X'pert HighScore Plus" PANalytical software. Quantitative results were obtained adopting the Rietveld method [33,34] where the standard parameters (crystal structure, crystallite size, diffraction optics effects and the instrumental factors) were refined. This computer code is implemented in the "Topas® Academic" software [35]. For this purpose 10 wt.% of analytical grade crystalline ZnO was added to the powder slag samples and homogenised by hand grinding in a mortar.

The hydraulic reactions were monitored by isothermal conduction calorimetry (TAM Air device, TA Instruments) at 20 °C. Analysis was performed on both as-received and milled slags for 2 h (LM slag only) and 6 h. The water to binder (i.e. solids) ratio (w/b) was equal to 0.5 for the as received slags and 1.0 for the milled material. The higher water demand for the milled slags is attributed to their increased specific surface area and was necessary in order to attain comparable viscosity, as observed by several authors on different materials, e.g. [28].

Based on the results obtained from the isothermal conduction calorimetry, the most reactive samples (i.e. highest cumulative heat release) were subjected to further analyses and tests to investigate the degree and the nature of the hydration reaction. The 6 h activated slag was mixed with water in 1:1 ratio, and stored in sealed plastic capsules up to 3, 7, 28 and 90 days. After the designated period of time, the samples were crushed to powder and the hydration was stopped by vacuum-drying (Alpha 1-2 LD, Martin Christ) for 2 h at 0.025 mbar, as suggested elsewhere [36].

The pulverised samples were subjected to thermal analysis using simultaneous TGA/DSC (STA 409 PC *Luxx*®, Netzsch). The samples were heated at 10 °C/min in a continuous N_2 flow up to 1000 °C. The vacuum-dried powder samples were mixed with α-ZnO as internal standard and analysed by QXRPD to follow the formation of the reaction products (conditions are described above). In order to analyse the hydration products, both 90 days hydrated paste samples and 6 h milled samples (as a reference) were analysed by Fourier transform infrared spectroscopy (Alpha spectrometer, Bruker). For the measurement, approximately 4.5 mg of the sample was hand ground, mixed with 450 mg of KBr and compressed into pellets. Microstructural investigation of the hydrated phases was performed using scanning electron microscopy (SEM XL30, Philips). For this purpose, bulk paste samples were dried in the oven at 50 °C for 2 days, based on the work by Knapen et al. [36] who demonstrated that these are optimal conditions minimising any microstructural changes. For the microchemical analysis, wavelength dispersive spectroscopy (WDS) was employed by means of a field emission microprobe (JXA-8530 F, Jeol). Elemental mapping was performed on 90 days hydrated mortar samples, after drying as described above. Analysis was performed on gold plated polished surfaces, by using an accelerating voltage of 10 kV in a 1024×1024 pixel area using the lowest possible sample moving step, i.e. 40 nm. Subsequent mineral maps were reconstructed based on the image stacking technique and greyscale separation for the specific minerals [37].

Both compressive and flexural strength was tested on mortar beams after 3, 7, 28 and 90 days (Instron 4467). The mortar beams were prepared according to EN 196-1 using CEN standard sand. The sand to binder ratio was kept 3:1. Both milled slags (LM, AOD) and reference OPC were used separately as binder to prepare the mortar samples. The amount of water needed to have adequate flow of the mortars was determined in accordance with EN 1015-3. Based on these results, the water to binder (w/b) ratio was adjusted to 0.5 for OPC and 0.75 for slag mortars. The OPC and slag mortars were cast in 20 mm×20 mm×160 mm moulds to obtain mortar beams for testing. These reduced dimensions, in comparison with standard moulds of 40 mm×40 mm×160 mm, were required due to the limited amount of slag obtained after the bead milling procedure. The mortar beams were stored at +20 °C and RH>95% until testing. Four measurements for compressive strength per mortar sample and hydration time were performed and the average values are reported.

Table 1
Chemical composition according to XRF of LM and AOD slag samples, in wt.%. F: not included.

Component	LM slag	AOD slag
CaO	51.5	55.6
SiO_2	28.3	31.7
MgO	11.3	9.8
Al_2O_3	1.2	1.2
Cr_2O_3	3.9	0.3
others	3.8	1.4

3. Results and discussion

3.1. Composition and phase analysis of as-received slags

The chemical composition of the AOD and LM slag is shown in Table 1. The main oxide equivalents in both slags are CaO, SiO_2, MgO, while Al_2O_3 and Cr_2O_3 are also present as minor constituents. Higher chromium content in the studied LM slag is possibly due to the additional alloying provided in the ladle with the aim of reaching the required chemical composition. Typically, LM slag has a chromium content below 1 wt.%.

Both investigated slag samples are basic, i.e. $M_b > 1$, according to the following formula:

$$M_b = \frac{(CaO + MgO)}{(SiO_2 + Al_2O_3)} \quad (1)$$

which results in a mainly crystalline slag [38]. The M_b values are 1.98 and 2.12 for AOD and LM slag respectively. The mineralogy of the slags determined by QXRPD analyses is summarized in Table 2.

Due to the relatively high magnesium content in the slags, the major phases besides γ-C_2S are merwinite, bredigite and periclase. These phases are generally considered as non-hydraulic or hydrating very slowly [39–41]. The formation of cuspidine [42], which is mainly formed in LM slag, was due to the addition of CaF_2 during refining. Among all the phases present, only β-C_2S is considered to be hydraulic, without additional activation, but in both samples its content is negligible.

3.2. Mechanical activation

3.2.1. Particle size distribution (PSD)

Fig. 1 (a) and (b) illustrates the particle size distribution of AOD and LM slag in the as-received state and after milling. The D_{50} of as-received slags equals approximately 19 μm and 55 μm for LM and AOD slag, respectively. After 6 h milling the D_{50} value decreased to 2 μm and 3 μm for LM and AOD slag, respectively. The results show that approximately 70 vol.% of the particles are below 10 μm in all samples after intensive milling, whereas in the as-receive state it was only 11 vol.% for AOD and 30 vol.% for LM slag respectively. The

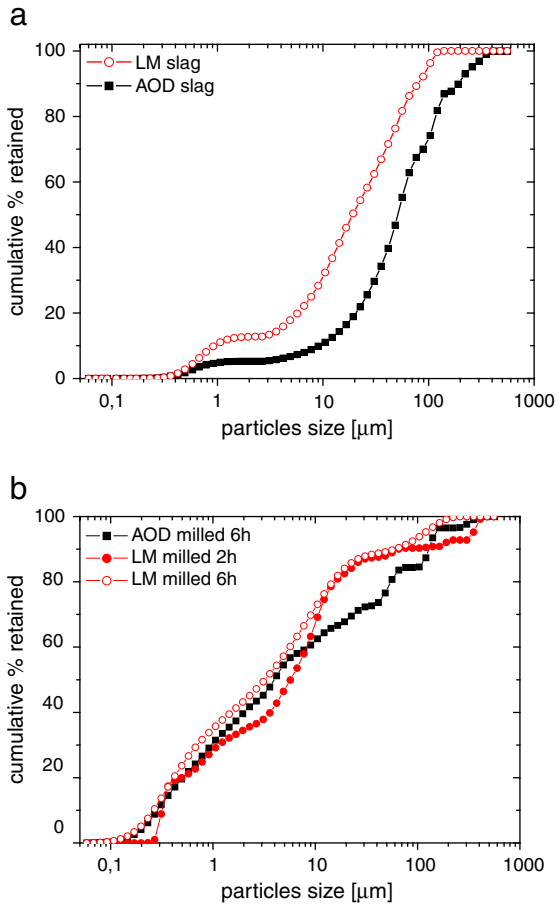

Fig. 1. Particles size distribution a) LM and AOD slag as received, and b) LM and AOD slag milled for 6 h.

Rosin-Rammler (RR) cumulative distribution for activated slags [43] was calculated as follows:

$$R = \left(1 - e^{-\left(\frac{D}{D_m}\right)^n}\right) \times 100\% \quad (2)$$

where R is the cumulative % retained at a size D, n is the size distribution constant, D is particle size and D_m is the mean particle size.

The statistical R-square value of the exponential fit for both samples is around 0.93 and therefore the exponential equation can be considered as a true representation of the cumulative particle size distribution. Thus, by comparing the two RR distribution curves it can be concluded that the milled powders are similar in terms of particles' populations and overall particle size distribution. The above findings are also of relevance with respect to particle packing and in the analysis of the compressive strength results.

The BET specific surface area of the 6 h milled slag has increased significantly: from a starting value less than 1 m^2/g, the specific

Table 2
Mineral composition of LM and AOD slag as received, in wt.%.

No.	Phase	Theoretical formula	LM	AOD
1	γ-dicalcium silicate	γ-$(CaO)_2SiO_2$	34	16
2	β-dicalcium silicate	β-$(CaO)_2SiO_2$	<1	n/a
3	Merwinite	$Ca_3Mg(SiO_4)_2$	6	37
4	Bredigite	$Ca_{1.7}Mg_{0.3}SiO_4$	7	15
5	Wollastonite	$CaSiO_3$	2	3
6	Periclase	MgO	15	7
7	Cuspidine	$Ca_4Si_2F_2O_7$	10	<1
8	Fluorite	CaF_2	2	4
9	Magnesiochromite	$MgCr_2O_4$	3	n/a
10	Others/Amorphous		20	18

Table 3
Specific surface area (m^2/g) determined by BET, cumulative (cml) heat release between 10 and 80 h of hydration (J/g) and ratio of the two (J/m^2).

	LM slag			AOD slag	
	as received	2 h milled	6 h milled	as received	6 h milled
Specific surface area (m^2/g)	0.7	5.6	9.7	0.9	8.1
Cml heat release (J/g)	3.4	30.6	61.1	1.7	51.9
Cml heat release/Specific surface area (J/m^2)	5.1	5.5	6.3	1.9	6.4

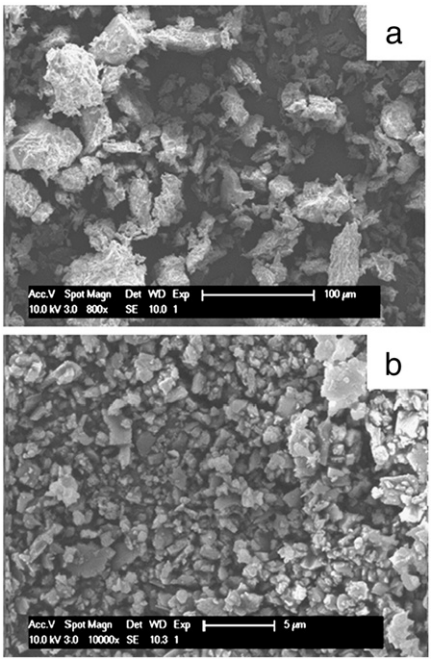

Fig. 2. SEM of a) AOD slag as received, and b) AOD slag milled for 6 h.

surface area became approximately 10 m^2/g for LM and 8 m^2/g for AOD slag after milling (Table 3). The shape of as-received particles and particles after milling is presented in SEM micrographs, Fig. 2. As-received slag powder consists mostly of irregularly shaped particles; C_2S grains in particular are characteristic in view of their extensive network of cracks. After 6 h of milling, the particles were smaller and angular.

3.2.2. X-ray powder diffraction analysis

The X-Ray diffraction patterns before and after milling are presented in Fig. 3, whereas results by Rietveld analysis are reported in Tables 2, 4 and 5. By comparing the patterns, one can see lower peak intensities and significant peak broadening for the milled sample. The peak broadening is caused by the structural disorder introduced during milling. Based on the quantitative data, the amount of γ-C_2S, merwinite, bredigite, periclase, fluorite and wollastonite decrease whereas the amount of amorphous phase increases upon milling. The different behaviour of the crystalline phases during milling depends on their specific fracture energy. Quantification of each mineral in the slag, before and after 6 h milling, reveal that γ-C_2S shows relatively higher degree of amorphisation, 30% in LM and 58% in AOD slag, compared to merwinite and bredigite. This is probably linked with the β→γ polymorphic transformations during cooling and the substantial stress generation and crack formation. Only wollastonite was found to be more susceptible to amorphisation due to milling, with 77% and 64% change in LM and AOD slag respectively.

3.3. Hydration

3.3.1. Heat of hydration by isothermal calorimetry

As demonstrated in Fig. 4, the slags in the as-received state showed only negligible or no heat release at the early stage. However, in both milled samples, a sharp exothermic peak occurred after 17 h and 25 h for LM and AOD slag respectively. These peaks are primarily associated with heat released due to hydration reactions; other dissolution reactions may be also contributing to a small extent. The cumulative energy released within the first 80 h (highest reaction rate) equals to 61 J/g for LM and 52 J/g for AOD milled slags. For comparison purposes, the heat released by OPC with BET surface lower than 1 m^2/g is around

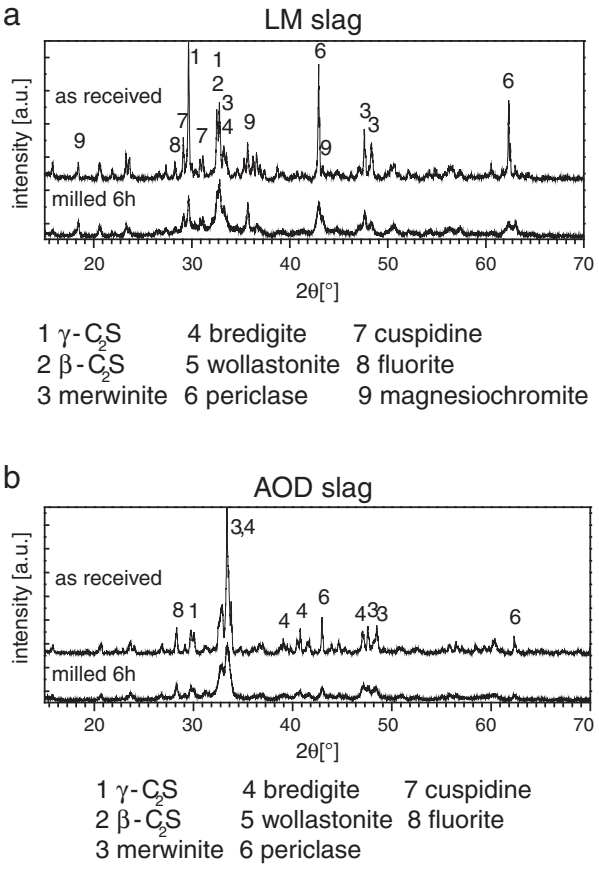

Fig. 3. XRD pattern of as-received powders and powders after 6 h milling a) LM slag, and b) AOD.

200 J/g (results not presented in Fig. 4). In Fig. 4(a), results from 2 h milling are also included. In this case, the total heat released is approximately 30 J/g, an indication that prolonged milling has a significant effect on the hydraulic reactivity.

The increased reactivity is a consequence of both increased specific surface area and of enhanced stored energy, resulting from the structural defects introduced during milling. This combined activation effect can be clearly seen by closer examination of the part of the graphs where the exothermic peaks are present, e.g. between 10 h and 80 h of hydration. It is calculated that the ratio of total heat release during the mentioned time period over the surface area of reacting powders (Table 3) increases gradually, an indication that the surface is not the only factor influencing the reactivity.

3.3.2. QXRD

As the C–S–H phase has a poorly crystalline structure that does not give clear diffraction peaks in XRD patterns [30,44], the hydration

Table 4
Evolution of phases during hydration for LM slag based on Rietveld analysis, in wt.%.

Phase	Milled 6 h	3 days	7 days	28 days	90 days
γ-dicalcium silicate	24	17	16	13	13
β-dicalcium silicate	4	<1	<1	n/a	n/a
Merwinite	5	4	3	3	2
Bredigite	6	4	4	2	<1
Periclase	12	6	4	1	<1
Cuspidine	12	8	9	7	7
Portlandite	<1	1	1	2	1
Brucite	n/a	1	2	3	3
Others/Amorphous	29	51	53	64	67

Table 5
Evolution of phases during hydration for AOD slag based on Rietveld analysis, in wt.%.

Phase	Milled 6 h	3 days	7 days	28 days	90 days
γ-dicalcium silicate	7	6	6	5	4
Merwinite	29	13	14	13	7
Bredigite	11	10	10	4	<1
Periclase	6	3	3	1	<1
Cuspidine	<1	<1	<1	<1	<1
Portlandite	<1	<1	<1	<1	<1
Brucite	n/a	<1	<1	2	2
Others/Amorphous	44	64	63	71	82

process could be indirectly tracked by monitoring the growth of the amorphous fraction [45]. The latter increased significantly with hydration time, Tables 4 and 5. After 28 days of hydration, the amorphous content was estimated at 64 wt.% and 71 wt.% for LM and AOD slag, respectively. In terms of crystalline phases, the major phases originally present in slag decrease with hydration time and new phases, being the reaction products of the occurring hydration, are detected (Tables 4 and 5). In particular, high reaction rates are recorded for β- and γ-C_2S, merwinite and periclase, especially for the first 3 days of hydration. Bredigite is also decreasing but at a slower rate. Regarding cuspidine, in LM slag, it decreases during the first 3 days then it remains stable; in AOD slag it is present in very low concentration which remains practically constant. New phases, CH, being the reaction product most probably of C_2S, and calcite, formed after the carbonation of CH, were detected. In addition, brucite gradually appears in the system resulting from the hydration of periclase. The quantity of brucite determined by QXRD is relatively low, despite the high initial content of periclase, and its content diminishes as hydration advances, which is an indication that it hydrates. The dilution effect in view of the increasingly bounded crystalline water can not suffice alone as an interpretation. Most probably the reaction product from periclase is poorly crystalline and/or the Rietveld quantification underestimates its content. As a result, in both events described above, a fraction from the hydration of periclase is calculated as amorphous phase in Tables 4 and 5. Thus, the amorphous phase alone should not be treated as a quantitative indication of C–S–H growth.

3.3.3. Thermal analysis

Thermogravimetry (TGA) and differential thermogravimetric analysis (DTG) are widely used for the monitoring of the hydration process and for the determination of the content of hydrated phases such as calcium silicate hydrate (C–S–H), calcium hydroxide (CH), etc [46,47]. In addition, the overall weight loss is informative on the hydration and carbonation extent. The TGA/DTG curves, Fig. 5(a), (b), shows indeed a number of characteristics peaks and an overall weight loss that increases as hydration times advances. The weight loss of both non hydrated slag samples is negligible compared to the hydrated ones, Fig. 5(a), (b). In more detail, Table 6, for LM slag the weight loss is 12.6%, 13.2%, 15.5% and 16.4% for 3, 7, 28 and 90 days of hydration respectively. Recalculation by dividing with the hydrating days (assuming linear weight gain over the designated periods) shows that the hydration rate, expressed in weight gain per day, is significantly higher the first 3 days. As hydration advances, hydration rates are gradually diminishing. A comparable trend is observed for AOD slag; weight loss is lower in this case, e.g. for 3 days is 11.2% and reaches 15.5% in 90 days. These findings are in

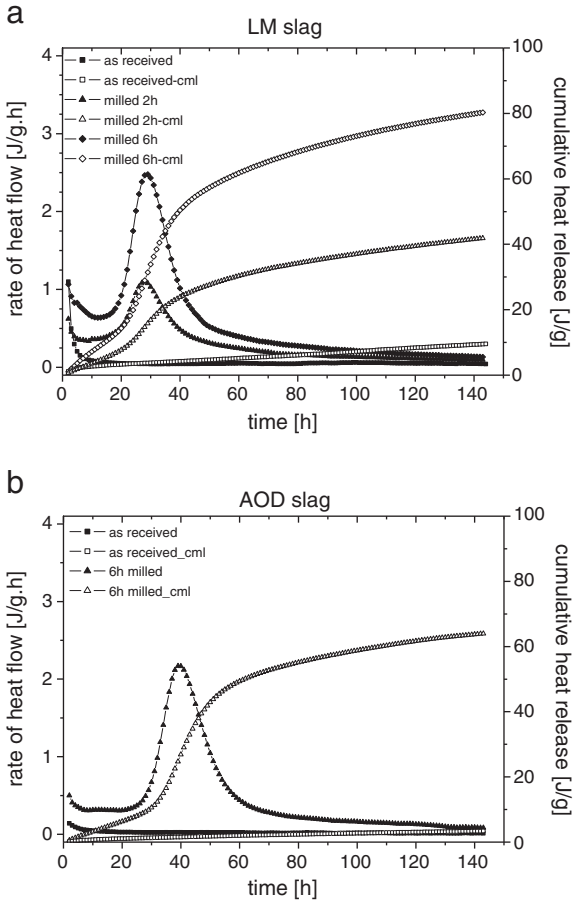

Fig. 4. Calorimetry measurements a) LM slag, and b) AOD slag; "cml" stands for cumulative.

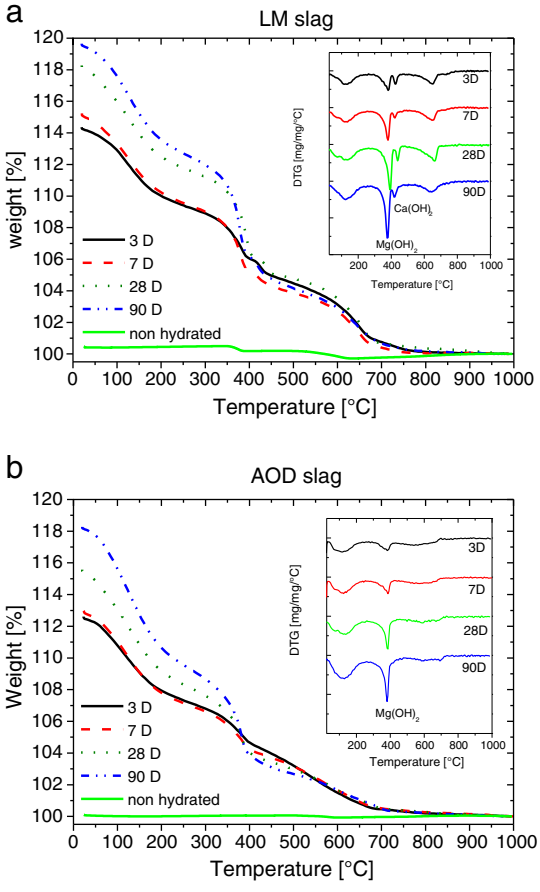

Fig. 5. TGA and DTG curves according to the ignited weight: a) LM slag, and b) AOD slag.

Table 6
Total weight loss and calculated amounts of CH and MH based on TG analysis, in wt.%.

Hydration time	LM slag			AOD slag		
	Weight loss	$Ca(OH)_2$	$Mg(OH)_2$	Weight loss	$Ca(OH)_2$	$Mg(OH)_2$
Non-hydrated	0.46			0.1		
3 days	12.6	1.8	4.2	11.2	n/a	2.6
7 days	13.2	1.0	6.8	11.5	n/a	3.6
28 days	15.5	2.0	9.7	13.5	n/a	6.2
90 days	16.4	1.8	10.0	15.5	n/a	9.1

agreement with XRD analysis, where high reaction rates were also observed for the first 3 days.

In terms of specific reactions, the TGA can be separated into the following parts: (i) 50 °C to 450 °C, weight loss associated with the decomposition of C–S–H [47] and possibly of other hydrates and hydroxides which might have been formed with the hydration of the amorphous phase formed upon milling; (ii) between 330 °C and 420 °C associated with the dehydration of brucite (MH) [48]; (iii) between 425 °C to 550 °C, associated with the dehydration of CH [29,49] and (iv) from 550 °C to 800 °C, ascribed to CO_2 volatilisation after the dissociation of calcite. Minor adaptations in the temperature ranges defined above might be needed depending on the specific TG response. The respective weight losses are reported in Table 6. Calculations were performed in accordance to the method proposed by Taylor [49], described in formula (3) for the dehydration of CH (changed accordingly for MH):

$$Ca(OH)_2[\%] = WL_{Ca(OH)_2}[\%] \times \frac{MW_{Ca(OH)_2}}{MW_{H_2O}} \quad (3)$$

where $WL_{Ca(OH)_2}$ is the weight loss during the dehydration of CH and $MW_{Ca(OH)_2}$ and MW_{H_2O} are the molecular weights of CH and water respectively.

In the case of LM slag, 1.8 wt.% of CH was determined after 3 days of hydration. This CH content stayed practically stable during the entire studied hydration period. Rietveld analysis gave comparable values, ranging from 1.4 wt.% for 3 days of hydration to 1.0 wt.% for 90 days of hydration. For AOD slag there is no peak in the TGA curve, in the temperature range 425 °C–550 °C, which could be associated with CH presence. This finding is in reasonable agreement with results from Rietveld analysis (Table 5), indicating CH content below 1 wt.%. The above findings are in accord with other works [50] as well, where comparable values between Rietveld analysis and TGA were found for CH.

For brucite (MH), results indicate high formation rates for both slags in the first 3 days of hydration and gradually diminishing rates as hydration progresses. In 90 days, approximately 9 wt.% and 10 wt.% of MH has been formed in AOD and LM slag respectively. As already commented, data from Rietveld analysis are not reflecting the expected MH formation and the present TG findings also verify the above (Table 6).

3.3.4. Fourier transform infrared spectroscopy (FT-IR)

Fig. 6 presents the FT-IR spectra of both LM and AOD slag after activation and after hydration for 90 days. A clear difference in the shape and depth of the peaks can be seen when the original slag was mixed with water. The presence of several phases makes the interpretation of the infrared spectra very complex as several peaks overlap. Still, some clear trends are observed. A sharp peak grows as the hydration progresses, at around 3680 cm^{-1} and 3640 cm^{-1}. This can be attributed to O–H stretching in CH and MH phases [51] that are formed with hydration reactions. The presence of carbonated phases, $CaCO_3$ and possibly (not detected by XRD) $MgCO_3$, is

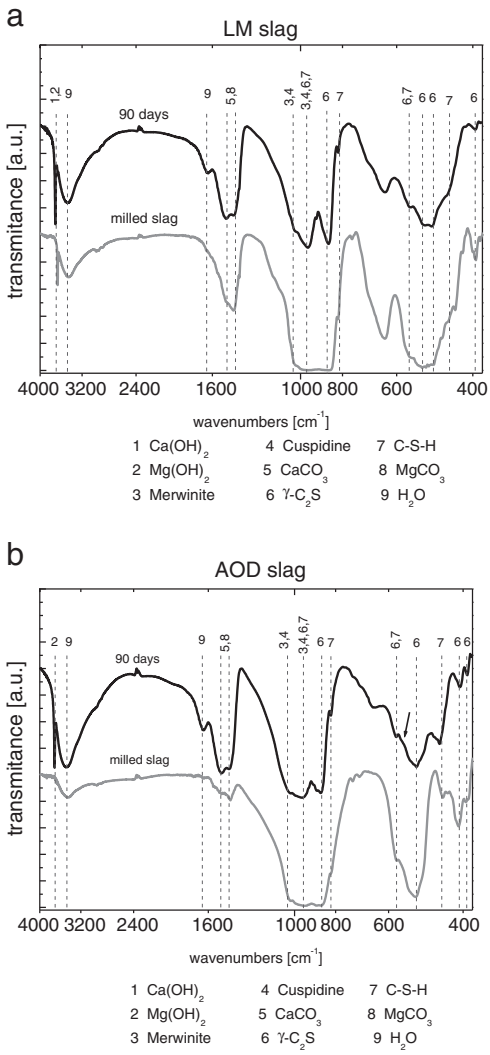

Fig. 6. FT-IR spectra of milled slag and slag hydrated for 90 days, a) LM slag, and b) AOD slag. The arrow indicates the tetrahedral MgO_4 deformation vibration.

evidenced by the sharp peaks at 1430 cm^{-1} and 1480 cm^{-1} [51]. The presence of these carbonates is also in-line with the TGA results, where weight loss occurs in the temperature range 500–700 °C. The vibration at 1650 cm^1 as well as a broad peak at 3450 cm^{-1} correspond to the O–H bond in H_2O molecule [52]. Vibrations in the region of 800–1200 cm^{-1} correspond to the asymmetric and symmetric stretching vibrations of Si–O bonds [53]. Peaks in this range are given by γ-C_2S, merwinite and cuspidine [51]. One can see a change of peak shape in this region for the hydrated slags. The originally rounded peaks are sharper and with lower intensity after the hydration. The same behaviour can be observed in the vibration range of 400–600 cm^{-1}. The vibrations at around 950, 815 and 560 cm^{-1} are generally assigned to the Si–O–Si bonds of poorly crystalline C–S–H gel. However, as mentioned elsewhere [53], in the presence of MgO, the structure of C–S–H gel can be modified, so that the calcium cation from the interlayer space is replaced by one magnesium cation with an octahedral coordination. Fernandez et al. [53] studied the effect of periclase presence on the hydration of C_3S and reported the tetrahedral MgO_4 deformation vibration at 530 cm^{-1}. A small shoulder is visible indeed in the AOD sample (marked by arrow). This could be an indication regarding Mg^{2+} incorporation in the gel structure. Regarding LM slag no shoulder in the suggested region was observed.

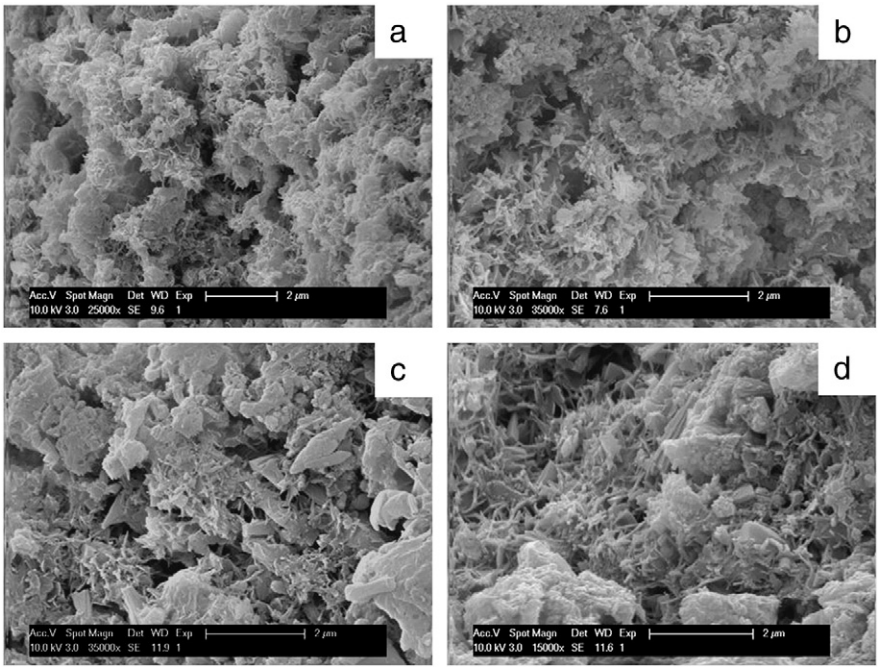

Fig. 7. SE micrographs of LM slag a) 3D, b) 7D, c) 28D and d) 90D.

3.3.5. SEM

C–S–H phase may exist in a variety of morphologies such as in the form of fibers, flakes, honeycombs, tightly packed grains or as a seemingly featureless dense material [48,54,55].

The hydration process of LM slag is monitored for the first 90 days, Fig. 7(a)–(d). These SEM images clearly show that gel-like structures resembling C–S–H phase have formed. LM slag hydrates with flake-like morphology at early stage growing to form a reticulated network at a later stage of hydration. In the case of AOD slag, the hydration starts with the formation of needles radiating from grains, forming spherical dense agglomerates as the hydration continuous. In both slags, the reticular network is visible even after 90 days of hydration. A substantial amount of porosity is present, especially in case of AOD sample. The morphology of crystals is more clearly visible in Fig. 8(a) and (b), for an AOD sample hydrated for 28 and 90 days respectively. Crystals of brucite are also detected in the microstructure.

The results of the microchemical analysis of LM sample after 90 days of hydration are presented in Fig. 9. Ca is widespread in the matrix, Fig. 9(b). Areas with a higher Ca concentration are attributed to CH; areas where Ca is practically absent correspond to grains of MgO and $MgCr_2O_4$. Si is also widespread in the matrix with minor concentration fluctuations, Fig. 9(c). Mg is present in the matrix, in the form of MgO, Mg $(OH)_2$ and/or $MgCO_3$ as well as $MgCr_2O_4$. The $Mg(OH)_2$ and/or $MgCO_3$ formations are typically encountered as a diffuse zone surrounding MgO, as expected in view of MgO hydration. The presence of $Mg(OH)_2$ is verified by both Rietveld (Tables 4 and 5) and TG analysis (Fig. 5); $MgCO_3$ is not identified in XRDs but its presence in small quantities cannot be excluded as TG graphs (Fig. 5) verify the presence of carbonates in the particular sample. $MgCr_2O_4$ are easily discernible due to the levels of Cr (data not presented). CaF_2 (no oxygen in elemental maps) exists in clear grains; cuspidine appears to be in small grains difficult to clearly resolve from the elemental maps (data not presented). The mineral distribution map constructed after the elemental maps, summarising the above analysis, is presented in Fig. 10.

The microchemical analysis above has not yet answered on the fate of Mg in the binding phase. Three possibilities are plausible: a) Mg forms M–S–H gel, in view of the knowledge that M–S–H and C–S–H gels are practically immiscible [56], b) a fraction of Mg is incorporated in the C–S–H gel [53,54,57] or c) Mg precipitates as $Mg(OH)_2$ or other hydroxides [56,58]. Evidently, the major obstacle is the very low particle size of the milled materials, considerably hampering the analytical accuracy. Despite the use of low moving step during the WDS mapping, analyses on the hydrates may be influenced from Mg-containing grains. Another factor relates to the heterogeneity of the materials. It is possible that locally established equilibrium may favour different reaction schemes. Apparently, the hydration products from the dissolution of merwinite will be different from that of

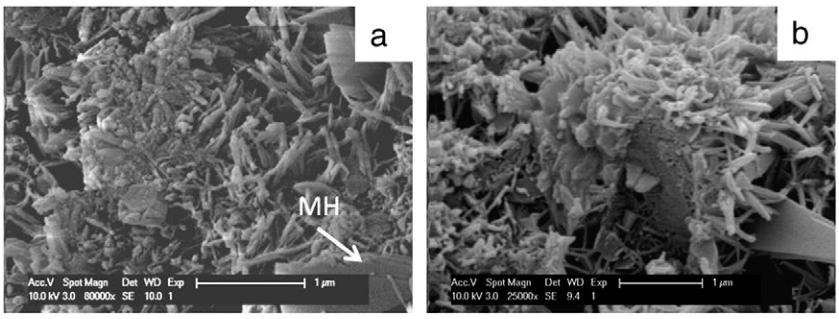

Fig. 8. Detail view on the hydrated C–S–H structure in AOD samples hydrated for a) 28 days, and b) 90 days.

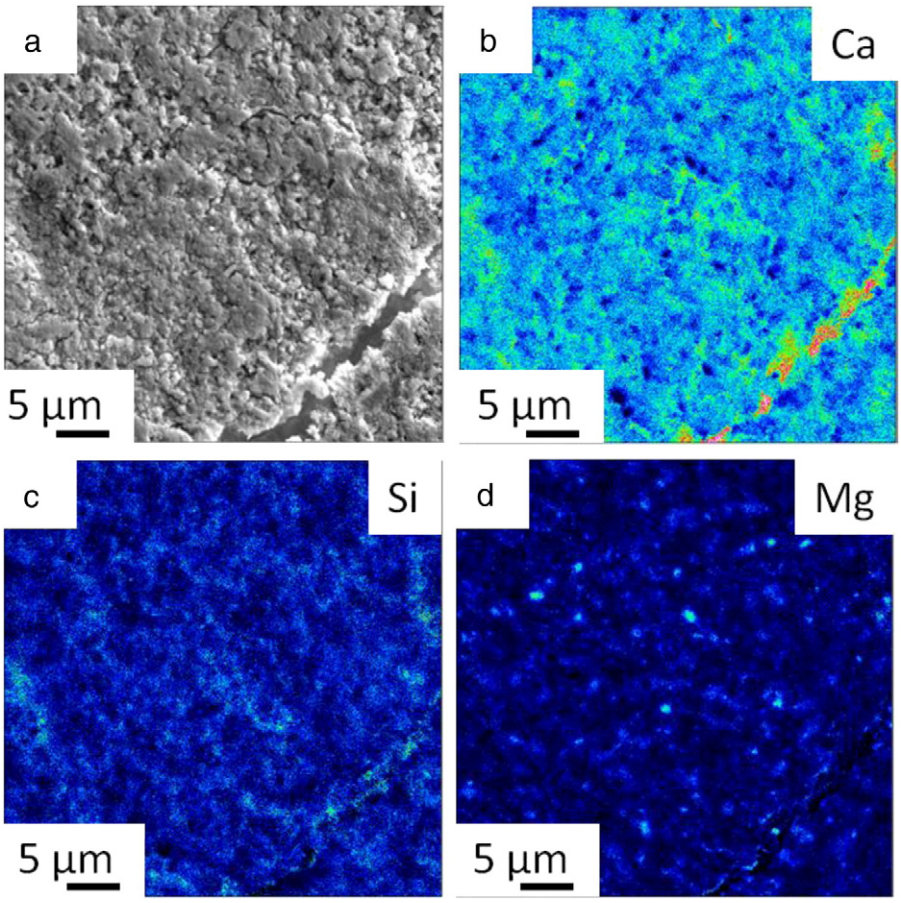

Fig. 9. Main element distribution according to WDS mapping on a 90 days hydrated LM slag mortar a) secondary electron image, b) Ca, c) Si and d) Mg.

periclase, or even, bredigite. As a conclusion, both the chemical availability and pH locally established will determine the preferred reaction path.

Focusing on the question posed above, image analysis was extended. Based on Fig. 10, all the identified grains/phases are excluded from the matrix. In accordance with XRD analysis, Table 4 and 5, the remaining phases are γ-C_2S, merwinite ($Ca_3Mg(SiO_4)_2$), bredigite ($Ca_{1.7}Mg_{0.3}SiO_4$), wollastonite ($CaSiO_3$), cuspidine ($Ca_4Si_2F_2O_7$) as well as the binding and other possible amorphous phases. Due to the chemistry and the fine particle size, the binding phase alone cannot be separated; however, the spatial distribution of areas with Ca and Si as well with Ca and Si and Mg per pixel, Fig. 11, is partially compensating for this. It results that formation of pure M–S–H is highly unlikely as Ca is widespread in the matrix. Regarding Mg incorporation in the C–S–H, analysis is not conclusive. There are indeed areas without Mg, but these areas may as well correspond to γ-C_2S or wollastonite ($CaSiO_3$). On the other hand,

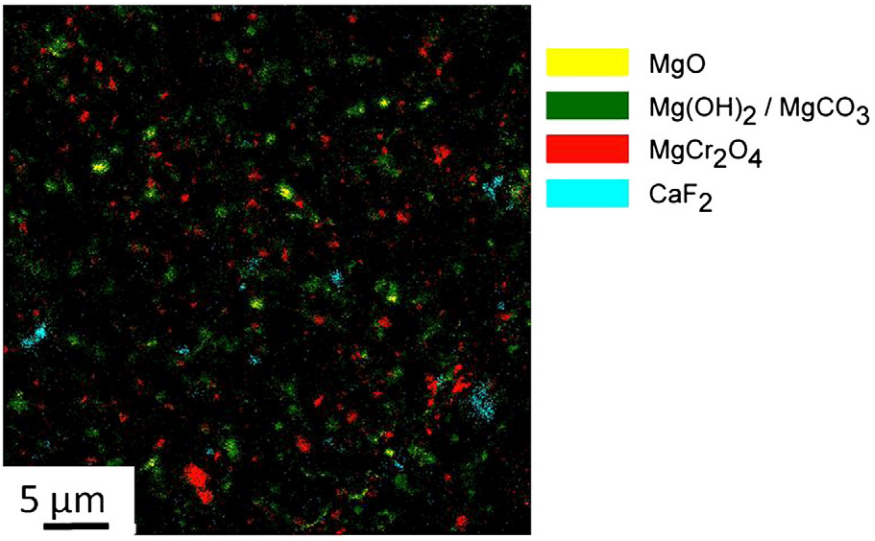

Fig. 10. Distribution of Mg, F and Cr containing phases.

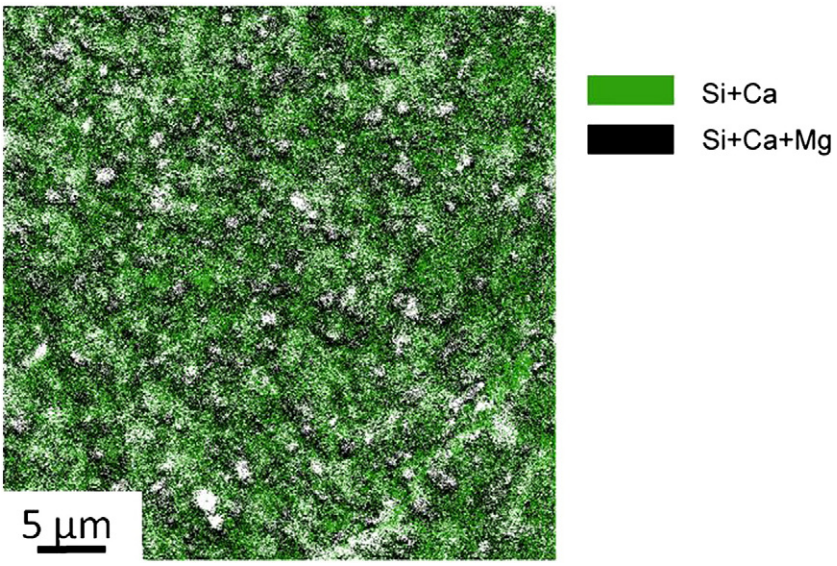

Fig. 11. Spatial distribution of areas with Ca and Si as well of areas with Ca and Si and Mg.

Ca and Si and Mg do co-exist, but these areas could be merwinite $Ca_3Mg(SiO_4)_2$ and bredigite, $Ca_{1.7}Mg_{0.3}SiO_4$.

3.3.6. Proposed reaction scheme

The reaction scheme proposed focuses on the behavior of main phases present, i.e. γ-C_2S, merwinite, bredigite and periclase. Results demonstrate that all these phases decrease significantly, especially during the first three days of hydration (Tables 4 and 5).

Gamma-C_2S, when activated, hydrates similarly to β-C_2S and forms C–S–H gel and CH [3]. Produced CH could act as a chemical activator in the next steps of hydration. As there was more γ-C_2S in LM slag compared to AOD slag, more CH was produced during hydration. The additional chemical activation caused by CH could be a reason for the higher reaction rate of γ-C_2S in LM slag compared to AOD. In both slags, the amount of CH does not increase with hydration time as it was expected. This phenomenon could be explained by the presence of MgO, which can hinder the precipitation of CH [53,59]. Results (Table 6) show that CH is mostly formed during the first three days of hydration and that the level stays relatively stable during the entire studied hydration period; on the contrary, the content of brucite increased gradually during the entire hydration period.

Regarding merwinite and bredigite, their hydration cannot be explicitly proven although their relative amounts decreased during hydration. Regarding merwinite, Muhmood et al. [45] observed that reducing the grain size enhances its dissolution kinetics in water and makes it highly hydraulic whereas Qian et al. reported that it hydrates under hydrothermal condition to form a Mg^{2+} containing C–S–H structure (Mg-calcio-chondrodite, tobermorite, Mg-gyrolite, Mg-truscottile and Mg-xonotlite) that strongly depends on the temperature and (C + M)/S ratio [57]. Similarly, the hydration of bredigite in an alkaline environment has been suggested before [41]. Still, no exact hydration reaction scheme has been described in the literature for merwinite and bredigite to the best of our knowledge.

Periclase reacts with water producing brucite ($Mg(OH)_2$). Generally, this reaction is slow and accompanied by volume increase causing "late swelling" effect [54]. In the present case, due to the fine particle size, the hydration kinetics are considerably fast and it is doubtful if periclase presence is indeed problematic.

3.4. Compressive strength

The results from both compressive and flexural strength measurements of the mortars are presented in Fig. 12. The mortars prepared with LM and AOD slag yield a gradual strength development up to 90 days due to the increased hydraulic activity attained after the mechanical activation.

The slag mortars indicated minor strength after 3 days of hydration that increased gradually up to 28 days. At 90 days, the compressive strength of the slag mortars reached 20% and 10% of an OPC mortar strength, for LM and AOD slag respectively. The flexural strength of

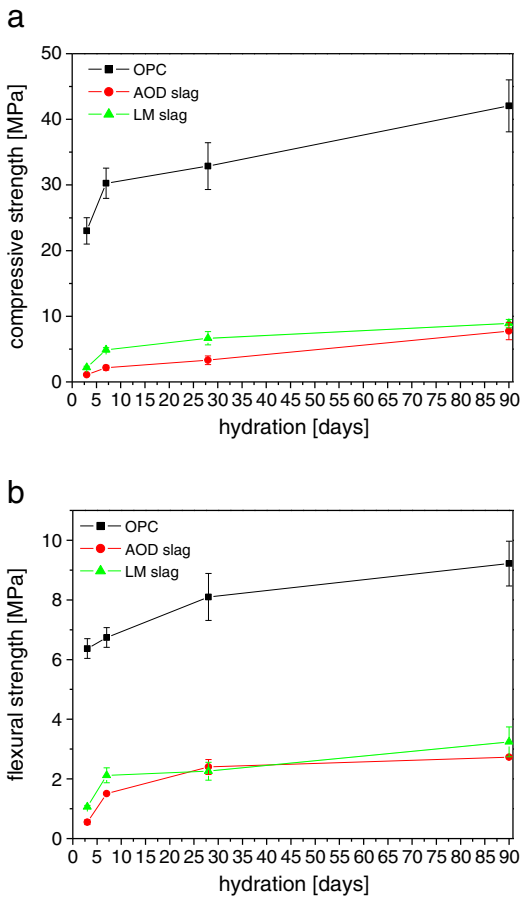

Fig. 12. Mortar strength: a) compressive, and b) flexural.

the mortars with activated slags reached 35% and 30% of the OPC mortar strength at the 90th day of hydration. Both flexural and compressive strength is higher when LM slag was used. This is probably due to the higher γ-C_2S content. As mentioned by P.V. Krivenko [9], γ-C_2S shows little cementitious properties and reaches approximately 5 MPa compressive strength for 90 days of hydration. This value is comparable with obtained results herein.

Nevertheless, the strength values are much lower than those of an OPC mortar. Obviously, the effect of w/b ratio on the mortar strength should be taken into account when comparing OPC and slag mortar samples. It is well known that porosity primarily depends on the degree of hydration and the w/b ratio, and that porosity of the hardened paste is strongly correlated with the strength [49]. Thus the higher w/b ratio used in the case of slag samples can have a negative effect on the mortar strength and should be optimised in further research.

4. Conclusions

1. Mechanical activation via prolonged milling caused the decrease of mean particle size to less than 3 μm and the increase of surface area by more than 10 times. In terms of structural changes, the XRD amorphous phase increased and γ-C_2S, merwinite, bredigite, periclase and fluorite decreased.
2. The mechanical activation significantly increased the reactivity of the slag when mixed with water. The amount of heat released per surface area increased with milling time, indicating that the surface is not the only factor influenc$_i$ng reactivity.
3. During hydration, the amount of C_2S, merwinite, bredigite and periclase decreased whereas brucite and the amorphous phase increased, indicating the hydraulic nature of the material.
4. The main hydration products according to TGA/DTG and SEM are most probably C–S–H gel, CH and MH. WDS mapping and FTIR results do not exclude Mg incorporation in the C–S–H gel structure of hydrated slag samples. Formation of M–S–H gel is unlikely as no pure Mg–Si regions were determined during WDS mapping.
5. Both slags showed cementitious properties and developed strength when mixed with water. The 90 days compressive strength reached 20% and 10% of OPC mortar strength for LM and AOD slag respectively. The 90 days flexural strength equalled 35%, for LM, and 30%, for AOD, of the OPC strength. However, these values can be further improved by optimising the w/b ratio.
6. Even though the hydraulic properties of both slags were significantly improved with mechanical activation, the developed strength is too small for most applications, if used alone as a binder.

Acknowledgements

The authors gratefully acknowledge IWT O&O project 090594 for the financial support. Y. Pontikes and Ö. Cizer are thankful to the Research Foundation - Flanders for the post-doctoral fellowship.

References

[1] H. Shen, E. Forssberg, U. Nordström, Physicochemical and mineralogical properties of stainless steel slags oriented to metal recovery, Resour. Conserv. Recycl. 40 (2004) 245–271.
[2] http://www.worldstainless.org/Statistics/Crude/,(1.12.2011.
[3] C. Shi, S. Hu, Cementitious properties of ladle slag fines under autoclave curing conditions, Cem. Concr. Res. 33 (2003) 1851–1856.
[4] Y.-M. Kim, S.-H. Hong, Influence of Minor ions on the Stability and Hydration rates of β-Dicalcium Silicate, J. Am. Ceram. Soc. 87 (2004) 900–905.
[5] I. Nettleship, K.G. Slavick, Y.J. Kim, W.M. Kriven, Phase Transformations in Decalcium Silicate: III, Effect of Barium on the Stability of Fine-Grained α'L and β Phase, J. Am. Ceram. Soc. 76 (1993) 2628–2634.
[6] Y.J. Kim, I. Nettleship, W.M. Kriven, Phase Transformations in Dicalcium Silicate: II, TEM Studies of Crystallography, Microstructure, and Mechanisms, J. Am. Ceram. Soc. 75 (1992) 2407–2419.
[7] J. Setién, D. Hernández, J.J. González, Characterization of ladle furnace basic slag for use as a construction material, Constr. Build. Mater. 23 (2009) 1788–1794.
[8] P.L. Cavallotti, C. Mapelli, F. Memoli, M. Pustorino, Recycling of LF-white slag, La Metallurgia Ital. (Ottobre 2007) 41–48.
[9] C. Shi, Characteristics and cementitious properties of ladle slag fines from steel production, Cem. Concr. Res. 32 (2002) 459–462.
[10] D. Durinck, F. Engström, S. Arnout, J. Heulens, P.T. Jones, B. Björkman, B. Blanpain, P. Wollants, Hot stage processing of metallurgical slags, Resour. Conserv. Recycl. 52 (2008) 1121–1131.
[11] Q. Yang, F. Engström, B. Björkman, D. Adolfsson, Modification study of a steel slag to prevent the slag disintegration after metal recovery and enhance slag utilization, Molten (2009) 33–41.
[12] H. Alanyali, M. Çöl, M. Yilmaz, Ş. Karagöz, Concrete Produced by Steel-Making Slag (Basic Oxygen Furnace) Addition in Portland Cement, Int. J. Appl. Ceram. Technol. 6 (2009) 736–748.
[13] The European Slag Association, Legal Status of Slag, Duisburg, GERMANY, 2006.
[14] L. Mihok, P. Demeter, D. Baricova, K. Seilerova, Utilization of ironmaking and steelmaking slags, Metalurgija 45 (2006) 163–168.
[15] M. Reuter, Y. Xiao, U. Boin, Recycling and environmental issues of metallurgical slags and salt fluxes, VII International Conference on Molten Slags Fluxes and Salts, 2004, pp. 349–356.
[16] Á. Rodriguez, J.M. Manso, Á. Aragón, J.J. Gonzalez, Strength and workability of masonry mortars manufactured with ladle furnace slag, Resour. Conserv. Recycl. 53 (2009) 645–651.
[17] R. Baciocchi, G. Costa, A. Polettini, R. Pomi, Influence of particle size on the carbonation of stainless steel slag for CO2 storage, Energy Procedia 1 (2009) 4859–4866.
[18] C. Duran Atis, C. Bilim, Ö. Çelik, O. Karahan, Influence of activator on the strength and drying shrinkage of alkali-activated slag mortar, Construct Build Mater 23 (2009) 548–555.
[19] J.S.J. van Deventer, J.L. Provis, P. Duxson, D.G. Brice, Chemical Research and Climate Change as Drivers in the Commercial Adoption of Alkali Activated Materials, Waste and Biomass Valorization 1 (2010) 145–155.
[20] Cement Technology Roadmap, Carbon emmision reductions up to 2050, World Business Council for Sustainable Development, 2009.
[21] http://www.iea.org/papers/2009/Cement_Roadmap_targets_viewing.pdf,(16.12.2011.
[22] W. Ruyi, C. Ronghuan, Beneficial use of stainless steel AOD slag as composite cement admixture and its safety analysis, Waste Recovery in Ironmaking and Steelmaking Processes, 2010.
[23] N. Faraone, G. Tonello, E. Furlani, S. Maschio, Steelmaking slag as aggregate for mortars: Effects of particle dimension on compression strength, Chemosphere 77 (2009) 1152–1156.
[24] U. Steinike, K. Tkacova, Mechanochemistry of Solids-Real Structure and Reactivity, J. Mater. Synth. Process. 8 (2000) 197–203.
[25] S. Kumar, R. Kumar, A. Bandopadhyay, T.C. Alex, B. Ravi Kumar, S.K. Das, S.P. Mehrotra, Mechanical activation of granulated blast furnace slag and its effect on the properties and structure of portland slag cement, Cem. Concr. Compos. 30 (2008) 679–685.
[26] C. Sasikumar, S. Srikanth, N.K. Mukhopadhyay, S.P. Mehrotra, Energetics of mechanical activation - Application to ilmenite, Miner. Eng. 22 (2009) 572–574.
[27] S. Kumar, R. Kumar, A. Bandopadhyay, Innovative methodologies for the utilisation of wastes from metallurgical and allied industries, Resour. Conserv. Recycl. 48 (2006) 301–314.
[28] N. Bouzoubaâ, M.H. Zhang, A. Bilodeau, V.M. Malhotra, The effect of grinding on the physical properties of fly ashes and a portland cement clinker, Cem. Concr. Res. 27 (1997) 1861–1874.
[29] S. Kumar, A. Bandopadhyay, T.C. Alex, R. Kumar, Influence of mechanical activation on the synthesis and hydraulic activity of calcium dialuminate, Ceram. Int. 32 (2006) 555–560.
[30] S. Kumar, A. Bandopadhyay, V. Rajinikanth, T.C. Alex, R. Kumar, Improved processing of blended slag cement through mechanical activation, J. Mater. Sci. 39 (2004) 3449–3452.
[31] P. Baláz, Extractive Metallurgy of Activated Minerals (Process Metallurgy), Elsevier Science, 2000.
[32] D. Tromans, J.A. Meech, Enhanced dissolution of minerals: stored energy, amorphism and mechanical activation, Miner. Eng. 14 (2001) 1359–1377.
[33] H.M. Rietveld, A method for including the line profiles of neutron powder diffraction peaks in the determination of crystal structures, Acta Crystallogr. 21 (1966) A228.
[34] H.M. Rietveld, A profile refinement method for nuclear and magnetic structures, J. Appl. Crystallogr. 2 (1969) 65–71.
[35] A.A. Coelho, TOPAS-Academic; A Computer Programme for Rietveld Analysis, 2004 http://wwwtopas-academicnet/.
[36] E. Knapen, O. Cizer, K. Van Balen, D. Van Gemert, Effect of free water removal from early-age hydrated cement pastes on thermal analysis, Construct Build Mater 23 (2009) 3431–3438.
[37] J.W. Lydon, The measurement of the modal mineralogy of rocks from SEM imagery: the use of Multispec © and ImageJ freeware, Geological Survey of Canada, 4941, 2005, p. 37, Open File.
[38] M. Tossavainen, F. Engstrom, Q. Yang, N. Menad, M. Lidstrom Larsson, B. Bjorkman, Characteristics of steel slag under different cooling conditions, Waste Manage. 27 (2007) 1335–1344.
[39] G.J. McCarthy, D.G. Grier, M.A. Wisdom, R.B. Peterson, S.L. Lerach, R.L. Jarabek, J.J. Walsh, R.S. Winburn, Coal Combustion By-Product Diadenesis II, Internation Ash Utilization Symposium, 1999, Kentucky, USA.

[40] D. Venkateswaran, D. Sharma, L. Muhmood, S. Vitta, Treatment and characterisation of electric arc furnace (EAF) slag for its effective utilisation in cementitious products, Global slag magazine, 2007 October.
[41] D. Moseley, F.P. Glasser, Properties and composition of bredigite-structured phases, J. Mater. Sci. 17 (1982) 2736–2740.
[42] J. Eriksson, B. Björkman, MgO modification of slag from stainless steelmaking, VII International Conference on Molten Slags Fluxes and Salts, The South African Institute of Mining and Metallurgy, 2004.
[43] http://www.codecogs.com/code/statistics/distributions/continuous/rosin_rammler.php.
[44] R. Snellings, G. Mertens, Ö. Cizer, J. Elsen, Early age hydration and pozzolanic reaction in natural zeolite blended cements: Reaction kinetics and products by in situ synchrotron X-ray powder diffraction, Cem. Concr. Res. 40 (2010) 1704–1713.
[45] L. Muhmood, S. Vitta, D. Venkateswaran, Cementitious and pozzolanic behavior of electric arc furnace steel slags, Cem. Concr. Res. 39 (2009) 102–109.
[46] G. Mertens, R. Snellings, K. Van Balen, B. Bicer-Simsir, P. Verlooy, J. Elsen, Pozzolanic reactions of common natural zeolites with lime and parameters affecting their reactivity, Cem. Concr. Res. 39 (2009) 233–240.
[47] M. Castellote, C. Alonso, C. Andrade, X. Turrillas, J. Campo, Composition and microstructural changes of cement pastes upon heating, as studied by neutron diffraction, Cem. Concr. Res. 34 (2004) 1633–1644.
[48] V.S. Ramachandran, R.M. Paroli, J.J. Beaudoin, A.H. Delgado, Handbook of Thermal Analysis of Constructions Materials, Noyes Publications, Norwich, USA, 2002.
[49] H.F.W. Taylor, Cement Chemistry, Academic press, London, UK, 1990.
[50] K.L. Scrivener, T. Füllmann, E. Gallucci, G. Walenta, E. Bermejo, Quantitative study of Portland cement hydration by X-ray diffraction/Rietveld analysis and independent methods, Cem. Concr. Res. 34 (2004) 1541–1547.
[51] J.A. Gadsen, Infrared Spectra of Minerals and Related Inorganic Compounds, Butterworths, UK, 1975.
[52] I. García Lodeiro, D.E. Macphee, A. Palomo, A. Fernández-Jiménez, Effect of alkalis on fresh C-S-H gels. FTIR analysis, Cem. Concr. Res. 39 (2009) 147–153.
[53] L. Fernandez, C. Alonso, A. Hidalgo, C. Andrade, The role of magnesium during the hydration of C_3S and C-S-H formation. Scanning electron microscopy and mid-infrared studies, Adv. Cem. Res. 17 (2005) 9–21.
[54] P.C. Hewlett (Ed.), Lea's Chemistry of Cement and Concrete, 2004.
[55] Structure and Performance of Cements, Spon Press, London, UK, 2002.
[56] D.R.M. Brew, F.P. Glasser, Synthesis and characterisation of magnesium silicate hydrate gels, Cem. Concr. Res. 35 (2005) 85–98.
[57] G. Qian, A. Li, G. Xu, H. Li, Hydrothermal products of the C3MS2-C12A7-MgO system, Cem. Concr. Res. 27 (1997) 1791–1797.
[58] T. Zhang, C.R. Cheeseman, L.J. Vandeperre, Development of low pH cement systems forming magnesium silicate hydrate (M-S-H), Cem. Concr. Res. 41 (2011) 439–442.
[59] L. Zheng, C. Xuehua, T. Mingshu, Hydration and setting time of MgO-type expansive cement, Cem. Concr. Res. 22 (1992) 1–5.